

---

1 **Efficient continuous land change monitoring with pyxccd and S-CCD**

2 **2.0**

3 Su Ye <sup>a, b</sup> \*, Yingchu Hu <sup>a, b</sup>, Tianjia Chu <sup>a, b</sup>

4

5 *a State Key Laboratory of Soil Pollution Control and Safety, Zhejiang University, Hangzhou*  
6 *310058, China*

7 *b Zhejiang Key Laboratory of Agricultural Remote Sensing and Information Technology,*  
8 *Zhejiang University, Hangzhou 310058, China*

9

10 This preprint is under peer review for Science of Remote Sensing

11

12

---

## Abstract

Continuous change detection from satellite time series requires algorithms that are robust to structural breaks, computationally efficient, and accessible for reproducible large-area processing. We present *pyxccd*, an open-source, cross-platform Python package for continuous land change monitoring based on dense satellite time series. This package provides high-performance implementations of the newly proposed S-CCD 2.0 and COLD (the latest version of CCDC), through C kernels wrapped by a user-facing Python API, with pixel- and tile-based workflows for operational mapping. Relative to earlier S-CCD implementations, S-CCD 2.0 introduces an anomaly-break hierarchical decision rule for coarse-resolution products and exposes latent state estimates for interpretable trend-seasonality decomposition. Using 6,488 independently interpreted Landsat disturbance plots, S-CCD 2.0 achieved disturbance-detection performance comparable to COLD, with maximum F1 scores of 0.653 for S-CCD 2.0 and 0.664 for COLD. S-CCD 2.0 reduced computation by 1.4-1.9x for retrospective processing and 3-6x for near-real-time updating, with larger gains as spectral dimensionality increased. Application examples across Landsat and coarse-resolution vegetation products demonstrate utilities of *pyxccd* for reproducible disturbance monitoring. This new tool lowers the technical barrier to scalable, near-real-time monitoring of land-surface change from dense satellite archives.

Keywords: Change detection, Time series analysis, Disturbance, State-space model, Near-real-time, Continuous Change Detection

---

## 34 1. Introduction

35 With the advancement of modern satellite technology, the frequency and spatial resolution  
36 of observations have been greatly improved, allowing for more granular data collection over  
37 time [1]. This has resulted in richer remotely sensed datasets capable of capturing subtle  
38 changes in environmental, climatic, and urban phenomena [2], [3], thus providing a more  
39 accurate and timely understanding of global trends. The increased density of remotely sensed  
40 data enables better tracking of short-term fluctuations as well as long-term trend analysis [4],  
41 [5], ultimately advancing our capacity to address pressing issues such as climate change [6],  
42 land use [7], and disaster monitoring [8].

43 Time series analysis of remotely sensed datasets is characterized by several unique features  
44 that distinguish it from other time-series application domains, such as finance and energy. First,  
45 many common time series tools, like Kalman filters [9] and Autoregressive Integrated Moving  
46 Average (ARIMA) models [10], assume that the system being modeled follows a predictable  
47 pattern with constant parameters, i.e., that the system is stationary. However, satellite-based  
48 time series are often interrupted by structural breaks caused by biophysical or biochemical  
49 processes (e.g., fires, degradation, phenological shifts, or ecological succession). When these  
50 breaks occur, statistical parameters, such as the mean, variance, circular patterns, or trends, may  
51 be significantly altered, requiring a break-aware behavior to reset the temporal and maintain  
52 model accuracy. Second, satellite-based time-series dataset is typically acquired at irregular  
53 intervals, influenced by factors such as satellite orbit schedules, cloud cover, and mission-  
54 specific objectives. This irregularity in data acquisition timing requires advanced techniques to  
55 manage and interpolate gaps in the data. In near real-time scenarios, gap filling must be

---

56 performed on-the-fly as new data arrives, which can cause detection delays when a longer  
57 dataset is needed to interpolate a missing observation. Third, the massive volumes of image-  
58 based time series datasets, often in the form of high-resolution images covering vast geographic  
59 areas over extended periods, present substantial computational challenges. Processing these  
60 billions of time series at a pixel level requires highly efficient storage solutions, optimized data  
61 processing pipelines, and sophisticated analytical methods to extract meaningful insights and  
62 support timely decision-making.

63       The Continuous Change Detection and Classification (CCDC) algorithm, first proposed by  
64 Zhu and Woodcock (2014), has gained widespread popularity as it continuously analyzes all  
65 clear observations in chronological order and updates the land-surface temporal model as new  
66 observations become available. Its descendants and operational implementations support  
67 continental to global land-cover and land-change products [12]–[16]. One key strength is its  
68 detecting temporal breaks as the first-class feature (i.e., break-aware), by examining spectral  
69 change magnitudes at each observation using a predefined threshold. These magnitudes are  
70 computed as the difference between the observed and modeled surface reflectance, normalized  
71 by Root Mean Square Errors (RMSE). After a break is confirmed, CCDC fits a trend-seasonal  
72 harmonic regression model to each resulting temporal segment, combining a linear trend with  
73 seasonal components represented by sine and cosine terms, and then uses the fitted multiband  
74 coefficients as features for subsequent land-cover classification. Because harmonic regression  
75 does not require equal temporal spacing, CCDC can operate directly on irregularly sampled  
76 observations without resampling or gap-filling, which is advantageous for sensors with  
77 moderate revisit frequency (e.g., Landsat and Sentinel-2) where 8-day or 16-day composites

---

78 are not consistently available. Notably, Google Earth Engine (GEE) has provided CCDC as a  
79 built-in function, enabling large-scale runs via cloud computing resources [17] and substantially  
80 reducing the engineering effort needed to process extensive image archives. However, the  
81 version of CCDC in GEE does not expose several new important refinements (e.g., mean  
82 included angle, disturbance break identification) introduced in the latest CCDC version aimed  
83 at land disturbance monitoring, named as “COLD” (COntinuous monitoring of Land  
84 Disturbance) [18]. In addition, GEE may be suboptimal for local deployments that require full  
85 on-prem control or tight integration. For example, the computation could be constrained by  
86 platform quotas and task limits, customization is bounded by the server-side API environment,  
87 and exporting large intermediate or final products can add overhead and operational friction  
88 related to authentication, networking, and pipeline orchestration.

89       Despite its proven effectiveness, CCDC itself is not well suited for near real-time (NRT)  
90 monitoring because it updates model coefficients by reconstructing the harmonic model from  
91 scratch. For the latest version of CCDC (i.e., COLD), Zhu et al. (2020) suggested the model  
92 updating frequency is per observation with ~10% higher F1 score than annual updating  
93 frequency, while later being changed to the 3% of the observation number that has not  
94 undergone updating with three observations as minimum for efficiency boosting purpose. This  
95 rebuilding strategy typically requires retaining and repeatedly accessing a long historical record,  
96 which increases storage demands and reduces the operational feasibility of NRT deployments.  
97 It is also computationally inefficient: re-reading archives and refitting models introduces  
98 avoidable latency and cost, undermining timely change detection. To address these limitations,  
99 Stochastic Continuous Change Detection (S-CCD) algorithm extends CCDC by reformulating

---

100 the seasonal-trend model in a state-space framework [19], where trend and seasonal terms are  
101 treated as stochastic, time-evolving states. S-CCD preserves the continuous-monitoring logic  
102 from CCDC/COLD in the sense that it still identifies temporal breaks, but differ in how they  
103 update the model: rather than refitting the harmonic model from scratch, S-CCD applies a  
104 Kalman filter to update state estimates recursively as each new observation becomes available.  
105 This short-memory formulation propagates only the current state and its uncertainty,  
106 eliminating the need to retain and revisit the full time-series archive and thereby improving  
107 both NRT feasibility and computational efficiency.

108       Beyond efficiency, state-space models in S-CCD allow for a dynamic representation of the  
109 system over time, with improved handling of temporal dependencies. In COLD, change  
110 detection relies on static thresholds on change magnitudes against the prediction from the fixed  
111 models, which can fail to adapt to varying patterns or trends in the data. In contrast, the state-  
112 space framework enables S-CCD to update the model dynamically based on new observations,  
113 ensuring that the model remains relevant as local fluctuations. This dynamic adaptation helps  
114 better accommodate gradual within-regime drift (e.g., phenological shifts) without triggering  
115 unnecessary model reinitialization, while still flagging true disturbances via statistically  
116 significant innovations (filter residuals). The resulting state estimates also provide an  
117 interpretable representation of evolving seasonal and trend behavior, supporting finer  
118 characterization of subtle, progressive change.

119       Although S-CCD was initially introduced in 2021, early applications focused primarily on  
120 forest disturbance monitoring, and its reported F1 score for a comprehensive land-cover dataset  
121 was lower than that of COLD [19]. Moreover, the initial release exposed only a low-level C

---

122 implementation and was limited to Linux, constraining accessibility, and broader adoption.  
123 Motivated by multiple mapping projects and sustained user feedback, we have substantially  
124 improved both the detection accuracy, hereafter referred to as S-CCD 2.0, and its usability  
125 through modern software engineering practices. To better support the user community, we  
126 developed *pyxccd*, an open-source, cross-platform Python package for scalable, continuous  
127 land change monitoring from satellite time series.

128 This manuscript makes four main contributions: (1) S-CCD 2.0 extends the original state-  
129 space formulation with an anomaly–break hierarchical decision rule and latent-state outputs;  
130 (2) *pyxccd* provides high-performance C implementations for popular CCDC-like algorithms  
131 (COLD and S-CCD 2.0) through a user-facing Python API; (3) COLD and S-CCD 2.0 are  
132 evaluated using 6,488 independently interpreted Landsat disturbance plots; and (4) pixel- and  
133 tile-level workflows demonstrate how the package supports reproducible NRT disturbance  
134 monitoring and large-area mapping. Together, these algorithmic improvements, open-source  
135 implementation, and reproducible workflows lower the technical barrier for researchers and  
136 operational agencies seeking to continuously analyze dense satellite archives for land change  
137 monitoring.

## 138 **2. Algorithms implemented in *pyxccd***

### 139 **2.1 COLD**

140 After screening out the observations flagged as cloud, shadow, and snow by Fmask [20],  
141 COLD can be described as proceeding in two stages [18]: model initialization and continuous  
142 monitoring.

---

### 2.1.1 Model initialization

Model initialization aims to establish a stable “no-change” baseline trajectory from an initial set of clear observations. COLD first defines an initialization window that satisfies minimum data requirements (at least 12 clear observations, spanning at least one year, with the largest gap shorter than one year), and then applies Tmask within that window to further remove residual cloud/shadow/snow contamination missed by Fmask. It fits a harmonic regression per inputted band using the LASSO regression. The fitted model is then subjected to a stability test designed to reject a window that likely straddle an undetected change. In COLD, this test combines the absolute slope term with the larger absolute prediction bias at the start or end of the window, i.e.,

$$Magnitude_{overall} = |l_{slope}| + \max\{|l_{start}| + |l_{end}|\} < threshold \quad (1)$$

If the window fails the stability test, COLD advances the window by one clear observation (dropping the earliest and adding the next) and repeats the fitting and testing until stability is achieved. Once a stable window is found, COLD additionally applies a “look-back” step to revisit earlier clear observations that were skipped during window shifting and include those that remain consistent with the current model. Finally, the baseline model is refit for the finalized initialization window, with trend plus three seasonal harmonics:

$$\hat{\rho}_{i,t} = a_{0,i} + c_{1,i}t + \sum_{k=1}^{n=3} (a_{k,i} \cos\left(\frac{2\pi k}{m}t\right) + b_{k,i} \sin\left(\frac{2\pi k}{m}t\right)) \quad (2)$$

Where  $i$  is the  $i$ th band,  $t$  is the ordinal date,  $a_{k,i}$  and  $b_{k,i}$  are the harmonic coefficients,  $k$  indexes the harmonic frequencies (annual, semiannual, and four-month cycles),  $m$  is the number of days per year ( $m=365.25$ ).

### 2.1.2 Continuous monitoring

---

165 After the initial baseline model is established, COLD performs break detection  
166 sequentially. For each newly acquired clear observation, COLD updates the current-segment  
167 harmonic model using all stable clear observations accumulated so far. The model is re-fit from  
168 scratch using lasso regression with penalty parameter  $\lambda$  (Fig. 1), which controls the L1  
169 regularization strength (shrinkage of coefficients). A smaller  $\lambda$  yields weaker shrinkage and a  
170 more complex model (higher overfitting risk), while  $\lambda = 0$  reduces lasso to ordinary least  
171 squares. In the *pyxccd* implementation,  $\lambda$  is suggested as 20 for Landsat-like reflectance scaled  
172 to  $[0, 10000]$ .

173 Using the updated model, COLD predicts band-wise reflectance for the new date and  
174 evaluates the deviation between the observation and prediction as a multi-band change vector  
175 using a peek window (Fig.1). For the  $x$ -th observation and the  $i$ -th band, the normalized residual  
176 is

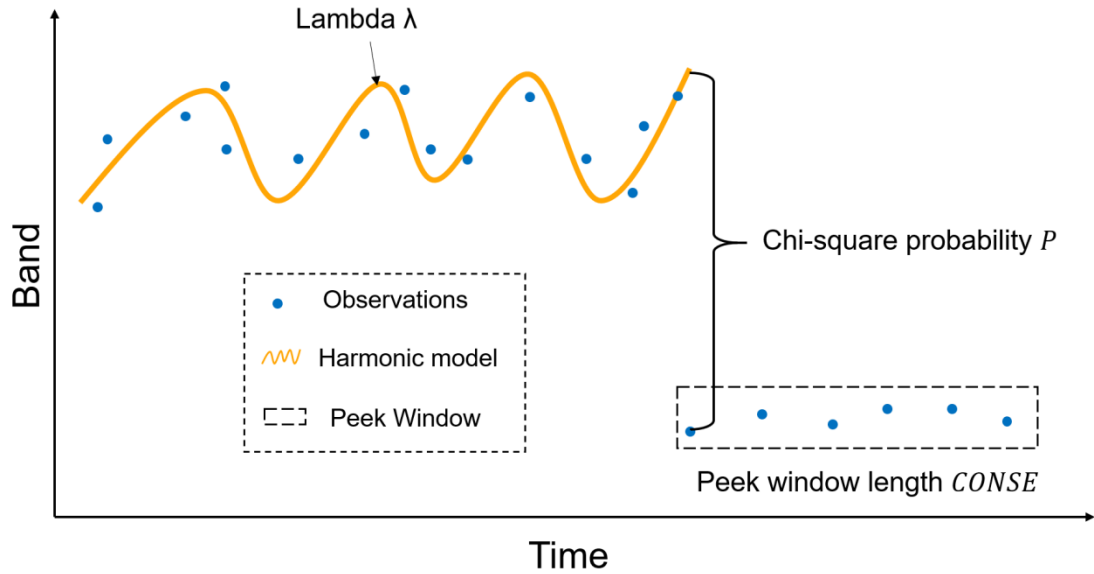
$$177 \quad cm_{i,x} = \frac{\rho_{i,x} - \hat{\rho}_{i,x}}{RMSE_{i,x}} \quad (3)$$

178 Where  $RMSE_{i,x}$  is the larger one between the temporally adjusted Root Mean Square Error  
179 (RMSE) and minimum RMSE that is lag-1 madogram for the time series [18]. The multi-band  
180 change magnitude is then defined as the squared norm of the normalized change vector:

$$181 \quad CM_x = \sum_{i=1}^k cm_{i,x}^2 \quad (4)$$

182 If each  $v_{i,x}$  is approximately standard normal, then  $CM_x$  follows  $\chi^2$  distribution with  $k$   
183 degrees of freedom, which allows COLD to set a statistically interpretable threshold using a  
184 change probability  $P$  (Fig. 1) (Typically  $P = 0.99$ ). A new observation is flagged as a break  
185 candidate when  $CM_x > \chi_k^2(P)$ . Using a strategy common to CCDC-like algorithms, COLD

186 employs a “peek window” approach to mitigate false alarms triggered by transient noise. A  
 187 break is only confirmed if candidates persist for a sequence of *CONSE* consecutive  
 188 observations (*CONSE* = 6 by default).



189

190 **Fig.1. Conceptual figure for three critical parameters for CCDC-like algorithms.**

191 Besides the change magnitudes, COLD applies a directional-consistency test by computing  
 192 included angles between neighboring normalized change vectors over the consecutive  
 193 anomalies. A break is confirmed only if the mean included angle is below a threshold (reported  
 194 as 45°). Once a change is confirmed, the break is recorded and the algorithm proceeds to  
 195 initialize the next temporal segment using post-break observations.

196 Unlike GEE-CCDC, COLD performs disturbance extraction after confirming a breakpoint,  
 197 converting generic spectral breakpoints into disturbance-oriented products by excluding false  
 198 positives, such as those associated with vegetation recovery. It uses a rule-based attribution  
 199 system that analyzes the direction of the multiband change vector and the model slopes before  
 200 and after the breakpoint. COLD identifies greener-direction breaks (NIR increases, Red and

201 SWIR1 decrease) as regrowth and classifies other breaks as land disturbances. For greener  
 202 breaks, it differentiates regrowth from reforestation or afforestation based on trend behavior,  
 203 producing three categories: disturbance, regrowth, and afforestation.

204 The differences between GEE-CCDC and COLD are summarized in Table 1.

205

206 **Table 1. Comparison between GEE-CCDC and COLD**

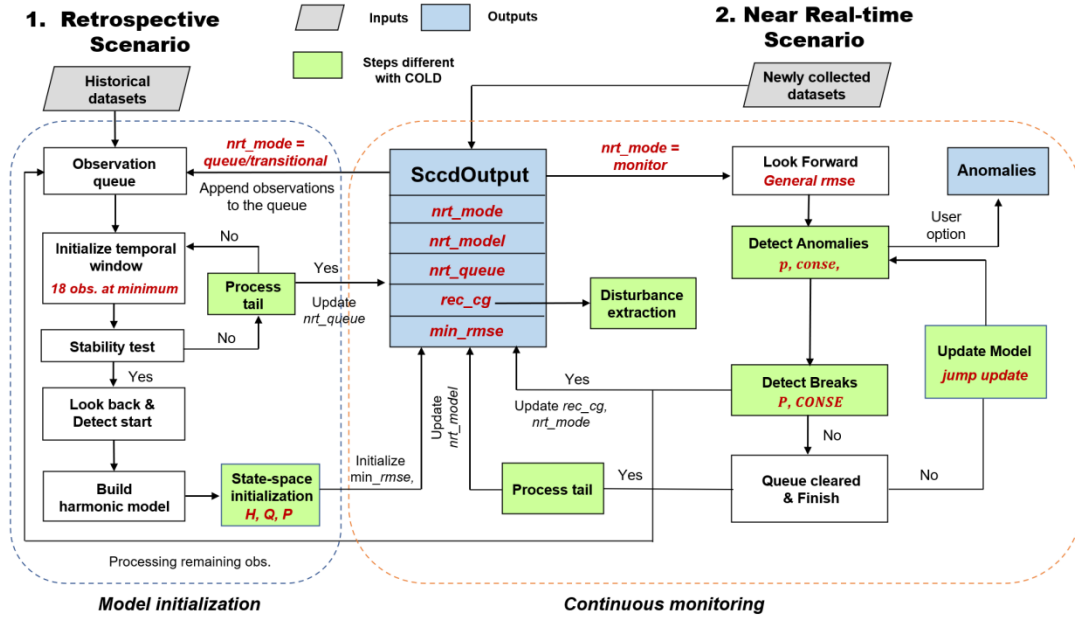
Steps	GEE-CCDC	COLD
Stability test	$ l_{slope}  + l_{start} +  l_{end}  < threshold$	$ l_{slope}  + \max\{ l_{start}  +  l_{end} \} < threshold$
Directional consistency check	None	Mean included angle test
Model update	Update by last fitting span days multiplied by 1.33	Update at each 3% of the observation number that has not been updated with three observations as minimum
Disturbance Extraction	None	Rule-based disturbance, regrowth, and afforestation attribution

207

## 208 **2.2 S-CCD 2.0**

209 S-CCD 2.0 builds upon the prototype introduced by Ye et al [19] and follows the same  
 210 two-step framework as COLD (Fig. 2). For retrospective scenario, S-CCD 2.0 processes  
 211 historical datasets in batch mode, with observations queued and analyzed after enough time-  
 212 series observations are collected. The retrospective scenario is used for backtracking historical  
 213 disturbance events to understand past behavior, or to prepare state-space model for the future  
 214 NRT usage. Differently, in the NRT scenario, S-CCD 2.0 continuously fed newly collected  
 215 datasets into the system at a certain monitoring frequency (e.g., weekly). S-CCD 2.0 will check  
 216 the current “status” of the pixel and choose to add them into the observation queue for model  
 217 initialization, or detect anomalies/breaks with the current state-space model for continuous

218 monitoring.



219

220 **Fig. 2. The workflow of S-CCD 2.0, which is newly proposed in this study.**

221 In the S-CCD 2.0 workflow, *SccdOutput* plays a critical role in managing and storing the  
 222 results of the monitoring and detection processes. It acts as a structured record that contains all  
 223 the necessary data for both model initialization and continuous monitoring. There are five key  
 224 elements in *SccdOutput*.

225 *nrt\_mode*: a two-digit integer describing predictability (first digit; 1 indicates no predictability)  
 226 and the current monitoring status (second digit). It helps informing predictability of the state-  
 227 space model, and track whether the system is in the process of initialization, monitoring real-  
 228 time data, or in a transitional state.

229 *nrt\_model*: a compact structure that stores the current state-space model when *nrt\_mode* is  
 230 monitor or transitional. It contains the updated model parameters that are used in the next  
 231 monitoring cycle, ensuring that the system always has the most recent information for detecting  
 232 anomalies and performing updates. See Table A1 in the appendix for details.

---

233 *nrt\_queue*: a structured array that stores incoming observations when *nrt\_mode* is queue. It  
234 allows the system to accumulate enough clear observations before reinitializing the state-space  
235 model.

236 *rec\_cg*: a structured array that records temporal segments and break information detected in the  
237 past according to the selected break thresholds (P and CONSE).

238 *min\_rmse*: an array containing the minimum RMSE for each band estimated during state-space  
239 model initialization. This value helps avoid unrealistically small errors for dark or shaded pixels  
240

### 241 **2.2.1 State-space initialization**

242 State-space models, the core mathematic foundation of S-CCD, explicitly model both  
243 observation and process uncertainties, which are key components for accurate change detection:

244 Observation equation:  $y_t = Z\alpha_t + \epsilon_t, \epsilon_t \sim \text{Normal}(0, H)$  (5)

245 Process equation:  $\alpha_{t+1} = T\alpha_t + \eta_t, \eta_t \sim \text{Normal}(0, Q)$  (6)

246 Here,  $y_t$  is the observation at time  $t$ ,  $\alpha_t$  is a state vector governing the system's evolution  
247 over time. S-CCD uses bimodal seasonal model (annual + semiannual), with six state variables  
248 by default:  $\mu_t$  (trend),  $v_t$  (trend),  $\gamma_{1,t}$  (annual),  $\gamma_{1,t}^*$  (annual),  $\gamma_{2,t}$  (semi-annual),  $\gamma_{2,t}^*$   
249 (semi-annual), where  $\alpha_t = (\mu_t, v_t, \gamma_{1,t}, \gamma_{1,t}^*, \gamma_{2,t}, \gamma_{2,t}^*)^T$ . To better accommodate the complex  
250 temporal variation, the users are opted to choose the trimodal (trend + annual + semiannual +  
251 four-month) in S-CCD 2.0. These states are transformed by the harmonic model from the  
252 initialization step (Eq. A1-A6 in Appendices). The system matrix  $Z$  indicates which state  
253 variables directly contribute to the observation (for six states):

---

254  $Z = [1, 0, 1, 0, 1, 0]$  (7)

255 Here, the states  $v_t$ ,  $\gamma_{i,t}^*$ ,  $\gamma_{2,t}^*$  serve as auxiliary states that are not directly involved in  
 256 observation calculation but are essential for recursive updates of the other states, therefore, their  
 257 weights were assigned as zero in  $Z$ .

258 The observation and process noise terms  $\epsilon_t$  and  $\eta_t$ , respectively, quantify the  
 259 uncertainties in the observation and the process model. Both are independent and normally  
 260 distributed, with variances  $H$  and  $Q$ , respectively. In S-CCD 2.0,  $H$  is assigned the RMSE of  
 261 the initial model, and  $Q$  is defined as a six-element vector corresponding to the six state  
 262 variables:

263  $Q = [q, \frac{q}{slope\_scale}, q, q, q, q]$  (8)

264 Where  $q$  is calculated as  $0.25 * \frac{LAM}{\lambda}$ , indicating the influence of the parameter  $\lambda$  on model  
 265 adjustments: Smaller values of  $\lambda$  increase the weight of fitting the actual observations, leading  
 266 to a higher  $q$  and better fit. The slope state  $v_t$  is scaled by  $slope\_scale$  (default value is  
 267 10,000,000), given that it typically has a lower numeric value than the other coefficients.

268 The transformation matrix  $T$  defines how the state vector evolves over time and is  
 269 determined by the harmonic components. For the bimodal seasonal model,  $T$  is as follows:

270  $T = \begin{bmatrix} 1 & 1 & 0 & 0 & 0 & 0 \\ 0 & 1 & 0 & 0 & 0 & 0 \\ 0 & 0 & \cos\left(\frac{2\pi}{365.25}\right) & \sin\left(\frac{2\pi}{365.25}\right) & 0 & 0 \\ 0 & 0 & -\sin\left(\frac{2\pi}{365.25}\right) & \cos\left(\frac{2\pi}{365.25}\right) & 0 & 0 \\ 0 & 0 & 0 & 0 & \cos\left(\frac{2\pi}{2*365.25}\right) & \sin\left(\frac{2\pi}{2*365.25}\right) \\ 0 & 0 & 0 & 0 & -\sin\left(\frac{2\pi}{2*365.25}\right) & \cos\left(\frac{2\pi}{2*365.25}\right) \end{bmatrix}$  (9)

271

272 A crucial parameter in the state-space model is the covariance matrix  $P$ , which

273 represents the uncertainty of the state variables. The initial covariance  $P_0$  reflects the  
 274 uncertainty of the initial state. For the Landsat surface reflectance product, an uncertainty of 5%  
 275 has been reported [21]. Accordingly, the uncertainties of the initial states are estimated as  $\lambda =$   
 276  $(\mu_0 * 5\%)^2$ . The initial covariance  $P_0$  is thus given:

$$277 \quad P_0 = \begin{bmatrix} \lambda & 0 & 0 & 0 & 0 & 0 \\ 0 & \lambda/slope\_scale & 0 & 0 & 0 & 0 \\ 0 & 0 & \lambda & 0 & 0 & 0 \\ 0 & 0 & 0 & \lambda & 0 & 0 \\ 0 & 0 & 0 & 0 & \lambda & 0 \\ 0 & 0 & 0 & 0 & 0 & \lambda \end{bmatrix} \quad (10)$$

278 Unlike COLD, which determines the minimum RMSE for the entire time series, S-CCD  
 279 2.0 calculates the lag-1 madogram based solely on the observations used during the  
 280 initialization stage. The minimum RMSE for each inputted band is retained in the output  
 281 (“*SccdOutput*”) and can be used for subsequent online monitoring.

### 282 **2.2.2 Detect anomalies & breaks**

283 Once the observation  $y_t$  enter the system, S-CCD predicts the value for the band  $i$  at  
 284 time  $t$  using the state vector:

$$285 \quad \hat{\rho}_{i,t} = Z\alpha_{i,t} \quad (11)$$

286 Subsequently, it calculates the change magnitude  $CM_x$  following the same procedure of  
 287 COLD following Eq. 3 and Eq. 4.

288 S-CCD 2.0 implements a two-level detection hierarchy, i.e., anomaly and break, to assess  
 289 each observation  $x$  within its peak window. This approach differs from most CCDC-like  
 290 methods, which focus exclusively on break detection (i.e., structural changes). The two-level  
 291 hierarchy enables detection of subtle, short-lived signals (e.g., drought-related spectral  
 292 responses) and enhances performance for noisy or coarse-resolution time series. This is

---

293 important in cases where weak anomalies provide useful information but do not require model  
294 re-initialization. In typical CCDC-like workflows, a break triggers model re-initialization,  
295 which often requires at least one year of post-change observations to stabilize the model [4].  
296 Frequent re-initialization disrupts continuous monitoring and complicates the NRT operation,  
297 because the absence of a stable model immediately after a break reduces temporal continuity  
298 and limits the interpretability of subsequent monitoring outputs.

299 To address this, we introduces unified monitoring workflow with two detection levels  
300 following [8]: (1) the anomaly level, which uses a sensitive configuration with three  
301 consecutive anomalies with a change magnitude larger than 0.90 chi-square probability ( $p =$   
302  $0.90, conse = 3$  by default), to inclusively detect all types of spectral anomalies without  
303 triggering model re-initialization; and (2) the break level, which uses a conservative  
304 configuration ( $P = 0.9999, CONSE = 8$  by default) to identify pronounced structural  
305 changes that justify model reset. We allowed users to customize  $p$ ,  $conse$ ,  $P$ ,  $CONSE$ .

306 We also improve some detailed steps for S-CCD 2.0. For the current *pyxccd* version  
307 (v1.0.2), S-CCD 2.0 calculates a general RMSE, which simplifies the calculation by focusing  
308 on overall error without adjusting it for temporal changes, as opposed to the recursive  
309 temporally-adjusted RMSE used in S-CCD 1.0 [19]. The general RMSE requires much fewer  
310 variables to store for updates, while the recursive RMSE in S-CCD 1.0 necessitates storing 122  
311 variables. The final RMSE is the larger one between the general RMSE and minimum RMSE  
312 obtained in the initialization stage. To enhance the performance for the general disturbances, S-  
313 CCD 2.0 adopted the exactly same step of directional-consistency test and disturbance  
314 extraction in COLD after anomalies and breaks are identified, as opposed to angular spread and

---

315 disturbance evidence only for forest disturbances proposed in the first version [19].

### 316 **2.2.3 Update model**

317 S-CCD leverages linear Kalman filter to update the harmonic model from the previous  
318 state-space parameter at a per-band basis, ensuring that the model is always up to date and  
319 reflective of current data. For band  $i$ , S-CCD estimates the filter state  $a_{t|t,i}$  which combines  
320 observations and model prediction based upon their uncertainty measurements, i.e., the  
321 observation noise ( $H_i$ ) and the covariance matrix for the states ( $P_{t,i}$ ):

$$322 \quad F_{t,i} = Z P_{t,i} Z^T + H_i \quad (12)$$

$$323 \quad K_{t,i} = P_{t,i} Z^T \quad (13)$$

$$324 \quad a_{t|t,i} = a_{t,i} + K_{t,i} F_{t,i}^{-1} v_{t,i} \quad (14)$$

325 Next, the model generates one-step-ahead predicts for the states and the covariance matrix for  
326 the next step:

$$327 \quad a_{t+1,i} = T a_{t|t,i} \quad (15)$$

$$328 \quad P_{t+1,i} = T(P_{t,i} - K_{t,i} K_{t,i}^T F_{t,i}^{-1}) T^T + Q_i \quad (16)$$

329  $a_{t+1,i}$  will be used to predict surface reflectance ( $\hat{\rho}_{i,t+1}$ ) for  $t + 1$  following Eq.11. In the  
330 case of missing observations at time  $t$ , the covariance matrix could be simply updated by the  
331 transformation matrix  $T$  and  $Q_i$ :

$$332 \quad P_{t+1,i} = T P_{t,i} T^T + Q_i \quad (17)$$

333 For  $m$  consecutive days that the observations are missing, this update process would need  
334 to be repeated  $m$  times, which could be computationally costly. To improve efficiency, we  
335 developed a “jump update” for Kalman filter to estimate missing-observation  $P_{t+1,i}$  more  
336 effectively. Mathematically, processing  $m$  consecutive missing-observation days is equivalent

337 to perform one-time regular update for a time series that has a revisiting cycle of  $m$  days.  
 338 Accordingly, S-CCD 2.0 recalculates a temporal transformation matrix for a time series with  
 339 an interval of  $m$  days:

$$340 \quad T^* = \begin{bmatrix} 1 & 1 & 0 & 0 & 0 & 0 \\ 0 & 1 & 0 & 0 & 0 & 0 \\ 0 & 0 & \cos\left(\frac{2\pi*m}{365.25}\right) & \sin\left(\frac{2\pi*m}{365.25}\right) & 0 & 0 \\ 0 & 0 & -\sin\left(\frac{2\pi*m}{365.25}\right) & \cos\left(\frac{2\pi*m}{365.25}\right) & 0 & 0 \\ 0 & 0 & 0 & 0 & \cos\left(\frac{2\pi*m}{2*365.25}\right) & \sin\left(\frac{2\pi*m}{2*365.25}\right) \\ 0 & 0 & 0 & 0 & -\sin\left(\frac{2\pi*m}{2*365.25}\right) & \cos\left(\frac{2\pi*m}{2*365.25}\right) \end{bmatrix} \quad (18)$$

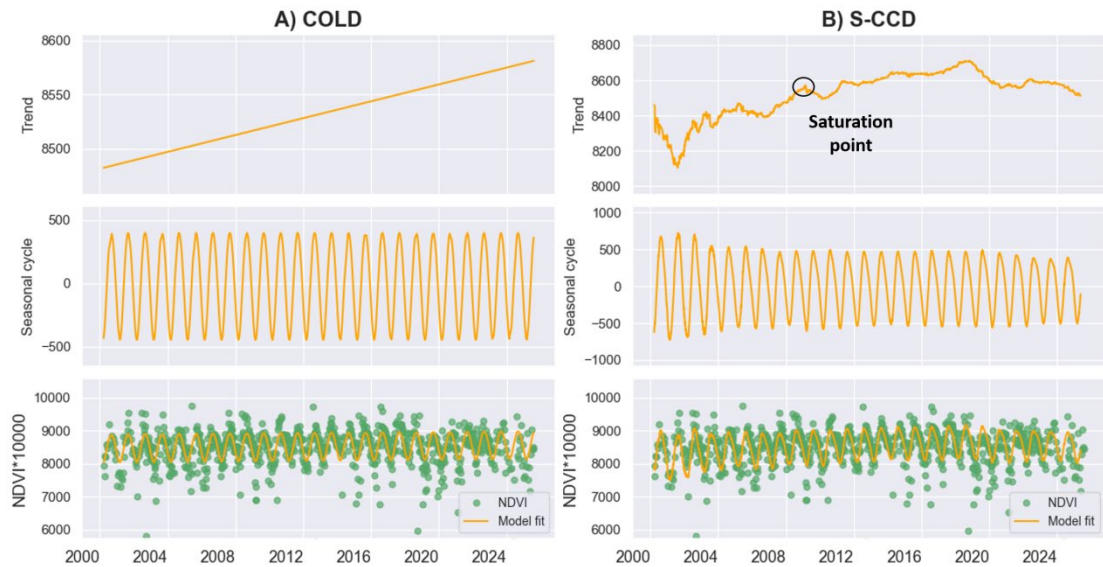
341 This allows for a one-time update using  $T^*$ , instead of  $m$  times (Eq. 19):

$$342 \quad P_{t+1,i} = T^*P_{t,i}T^{*T} + Q_i \quad (19)$$

343 Particularly, the state variables ( $a_{t,i}$ ) are scientifically useful because they transform a  
 344 noisy observation time series into an interpretable, continuously updated decomposition of  
 345 ecosystem dynamics, separating components such as the seasonal baseline and the slowly  
 346 varying level/trend. Fig. 3 compares the decomposition results from COLD (whose predictions  
 347 rely on fixed harmonic coefficients) and S-CCD 2.0 (whose outputs are the estimated states),  
 348 for the MODIS NDVI time series. Both methods recover a seasonal cycle and provide a model  
 349 fit to the observations, but they differ markedly in their characterization of the long-term  
 350 trajectory. COLD summarizes the record as a monotonic and linear increase, which can mask  
 351 subtle curvature in the underlying trend. In contrast, S-CCD 2.0 yields a more adaptive,  
 352 continuously evolving trend that highlights a gradual greening rise followed by a clear  
 353 saturation/flattening (“saturation point”) and subsequent slow variations. As a result, S-CCD  
 354 2.0 is particularly well suited for inspecting slowly varying trends, since it can track progressive,  
 355 non-linear changes that may be smoothed over or misrepresented when the trend is constrained

356 to a single linear form.

357



358

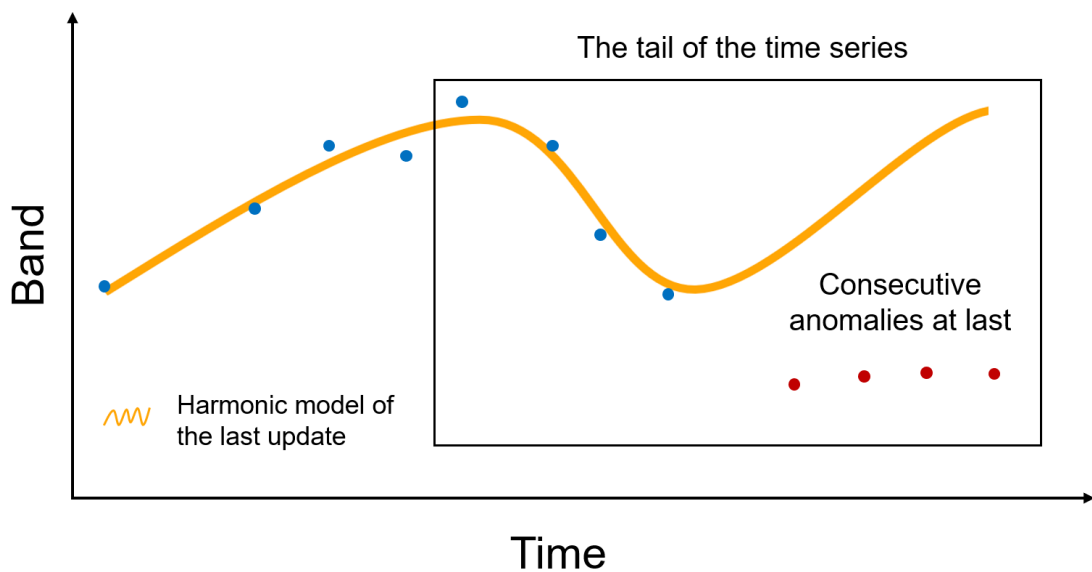
359 **Fig. 3. MODIS-based NDVI Time-Series decomposition for analyzing greening trend over**  
360 **a location of Tibet, China, illustrating that “states” of S-CCD 2.0 could be used to identify**  
361 **slowly varying trend/seasonality.**

### 362 2.2.4 Process tail

363 The final step of S-CCD 2.0 processes the tail end of the time series (Fig. 4), specifically  
364 the last CONSE observations, and saving all results into *SccdOutput*, for the next monitoring  
365 cycle, which includes new observations. There are three possible statuses for the tail  
366 observations (the second digit of the *nrt\_mode* parameter): *monitor*, *queue*, and *transitional*  
367 *Mode*.

368 *Monitor Mode*: the state-space model has been initialized. We are allowed to update a  
369 dictionary-like structure *nrt\_model* (see Table A1 in the appendix), retaining key parameters  
370 for future monitoring and updates (e.g., the peak window for the next update, state-space model  
371 parameters, and the sum of squared errors). The model can process newly incoming

372 observations with the parameters kept in *nrt\_model*. S-CCD 2.0 additionally extract  
373 information into in *nrt\_model* for consecutive anomalies at last (Fig. 4), as they often signify  
374 ongoing disturbances which has not satisfied the consecutive number required for identifying a  
375 break. Machine learning techniques can be further applied to these anomalies at the tail for NRT  
376 agent classification.



377  
378 **Fig. 4. S-CCD 2.0 processes the tail of the time series and reports the status for the**  
379 **consecutive anomalies at the last (dashed rectangle).**

380 *Queue Mode*: the state-space model is not initialized yet, so S-CCD 2.0 continues to collect  
381 new clear observations into *nrt\_queue*. Once new observations arrive, the system combines  
382 them with the stored observations from *nrt\_queue* to perform a stability test to determine if a  
383 state-space model can be established.

384 *Transitional Mode*: designed for practical NRT monitoring tasks with weekly or bi-weekly  
385 update frequencies, the *transitional* mode is triggered right after a break is detected. Practically,  
386 users require recent anomaly information for a period to generate spatially consistent maps after

387 the break. To accommodate this, S-CCD 2.0 retains *nrt\_model* for two weeks following the  
 388 transition from *monitor* to *queue* mode, allowing an NRT analysis on the recent anomalies even  
 389 they are not from the last update.

390 Additionally, the first digit of the *nrt\_mode* parameter indicates the predictability, with “1”  
 391 indicating no predictability and “0” meaning predictability. We conducted a predictability test  
 392 for both *monitor* and *transitional* modes to ensure that the state-space model remains stable  
 393 after the last anomaly is confirmed as a disturbance (for *queue* mode, unpredictability is always  
 394 set). The problem arises when a disturbance process persists for several weeks or months, such  
 395 as construction. In such cases, ambiguous anomalies may be continuously generated, as surface  
 396 reflectance during an event can be unpredictable. To address this, we designed a test to assess  
 397 the predictability of the state-space model. The model is considered predictable if the change  
 398 magnitudes of half the observations in the peak window are smaller than the critical value  
 399  $\chi_k^2(\text{predictability\_pcg})$ . The default *predictability\_pcg* set to is 0.90. Users can choose  
 400 to exclude ambiguous anomalies based on the outcome of the predictability test.

401 Overall, S-CCD 2.0 made substantial modifications on S-CCD first proposed, summarized  
 402 in Table 2.

403  
 404

**Table 2 Comparison between S-CCD [19] and the newly proposed S-CCD 2.0**

	S-CCD 1.0 [19]	S-CCD 2.0
State structure	Five states (no slope): $\mu_t, \gamma_{1,t}, \gamma_{1,t}^*, \gamma_{2,t}, \gamma_{2,t}^*$	Six states (or eight states as option): $\mu_t, \nu_t, \gamma_{1,t}, \gamma_{1,t}^*, \gamma_{2,t}, \gamma_{2,t}^*, \gamma_{3,t}, \gamma_{3,t}^*$
RMSE	Recursive temporally-adjusted RMSE	General RMSE
Detection	Only detect breaks	Detect both anomalies and breaks
Directional-consistency	Angular spread	Included angle (COLD’s approach)
Disturbance extraction	Combined evidence from multiband change magnitudes	Examination on individual change magnitudes (COLD’s approach)

---

Model updates	Covariance updates for each date regardless of missing observation	Jump covariance update for continuous missing observations.
Process tail	None	Perform additional predictability test; identify and save current mode

---

405

### 406 **3. Software implementation**

407 *Pyxccd* is an open-source, PyPI-installable Python package that bridges low-level  
408 computational performance with high-level scientific utility ([https://github.com/Remote-](https://github.com/Remote-Sensing-of-Land-Resource-Lab/pyxccd)  
409 [Sensing-of-Land-Resource-Lab/pyxccd](https://github.com/Remote-Sensing-of-Land-Resource-Lab/pyxccd)). It succeeds the MATLAB-based COLD  
410 implementation and serves as the primary platform for S-CCD 2.0 algorithms. Designed for  
411 both developers and researchers, *pyxccd* provides a flexible and scientifically rigorous  
412 environment for processing multi-sensor time-series datasets, moving beyond the fixed  
413 Landsat-band structure of the original CCDC framework.

414 The software architecture focuses on two key imperatives: computational throughput and  
415 modular flexibility.

416 *Hybrid C-Python Core*: at its core, *pyxccd* integrates C-based computational kernels to  
417 handle tasks like iterative Lasso regression and Kalman filtering, essential for the COLD and  
418 S-CCD 2.0 algorithms. Offloading these computational tasks to C ensures minimal memory  
419 overhead and high execution speed, making *pyxccd* suitable for both local workstations and  
420 distributed High-Performance Computing (HPC) clusters. Python acts as the interface layer,  
421 leveraging Cython and NumPy C-APIs for low-latency data exchange between the user  
422 interface and execution engine. This hybrid approach allows *pyxccd* to achieve much faster  
423 processing than pure Python implementations while offering an intuitive API.

---

424            *Modular Functional Design: pyxccd* employs a modular architecture that separates core  
425 detection logic from data I/O, time-series processing, and spatial orchestration. This allows  
426 specialized resource allocation, such as isolating numerical computations from data  
427 management tasks, and enables “lazy loading”, where only relevant data segments are loaded  
428 into memory. The modularity also allows for easy adaptation to the evolving remote sensing  
429 landscape, supporting various satellite data formats (e.g., HLS, MODIS, Planet) without the  
430 need for a complete re-engineering of the pipeline. We presented the details for the module  
431 designs in Appendix A2.

432

## 433 **4. Evaluation**

### 434 **4.1 Testing dataset**

435            We evaluated the accuracy and computational efficiency of COLD and S-CCD 2.0 for  
436 detecting disturbance-related breaks using an identical reference dataset. Specifically, we  
437 adopted the 7,200 disturbance plots from Conterminous United States used in the COLD study  
438 by Zhu et al. (2020). Their disturbance dates were originally interpreted by Cohen et al. (2016)  
439 based on Landsat time series, high-resolution imagery and ancillary datasets. Zhu et al. (2020)  
440 subsequently refined this reference database by excluding plots with insufficient clear-sky  
441 observations or high interpretation uncertainty. Following this refinement, a total of 6488  
442 Landsat plots were retained and used as testing samples in this study.

443            For the accuracy assessment, all available Landsat observations (Landsat 4, 5, 7, and 8)  
444 acquired between 1983 and 2017 were collected on a per-plot basis. For plots covered by two  
445 adjacent orbital paths, only the dominant path was retained to avoid duplication. The accuracies

---

446 of the COLD and S-CCD 2.0 were evaluated by analyzing the trade-off between omission errors  
447 and commission errors across three critical parameters ( $P$ ,  $CONSE$ ,  $\lambda$ ). We summarized overall  
448 accuracy using the F1 score, which provides a balanced measure of omission and commission  
449 errors.

450 To assess computational efficiency, we controlled for differences in observation density by  
451 randomly selecting 300 temporal observations for each plot; plots with fewer than 300  
452 observations were excluded from the analysis. Performance was evaluated across band numbers  
453 ranging from 1 to 10 for both the retrospective and NRT scenarios. In the retrospective scenario,  
454 computational performance was assessed using the two *pyxccd* functions that support user-  
455 defined band inputs: *cold\_detect\_flex()* and *sccd\_detect\_flex()*. In the NRT scenario, we  
456 compared *cold\_detect\_flex()* with *sccd\_update\_flex()* following the initial execution of  
457 *sccd\_detect\_flex()*, representing recursive model updating. When the specified number of bands  
458 exceeded the available Landsat bands, existing bands were replicated to maintain consistent  
459 input dimensionality. Computational efficiency was quantified as the average processing time  
460 per plot. All efficiency experiments were conducted on a desktop workstation running Windows  
461 11 Pro 64-bit, equipped with a 13th Gen Intel® Core™ i7-13700 CPU, 64 GB RAM, and an  
462 SSD for local data storage. The experiments used Python 3.11.9, NumPy 2.3.4, and *pyxccd*  
463 v1.0.2. The evaluation script with the guidance for downloading testing dataset  
464 (*accuracy&efficiency\_test.ipynb*) is available at <https://github.com/Remote-Sensing-of-Land-Resource-Lab/pyxccd/tree/devel/tutorials/notebooks>.  
465

466

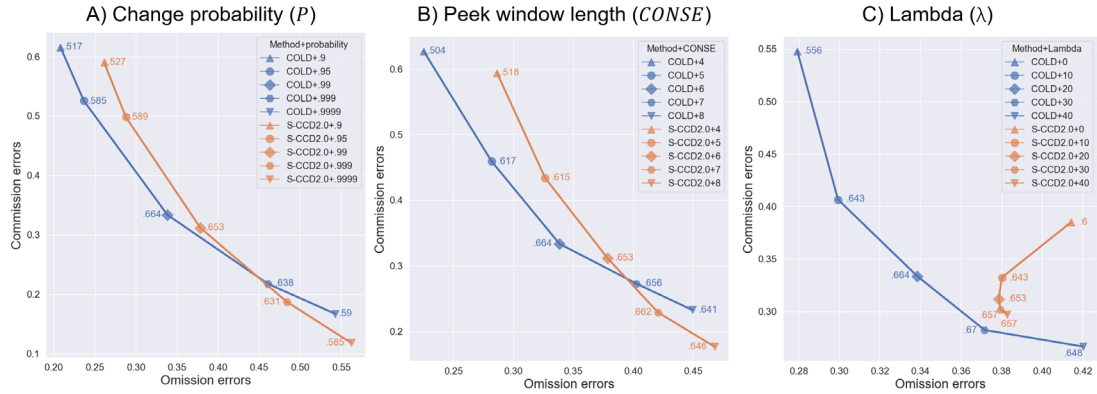
## 467 4.2 Results

---

468 Fig. 5 illustrates the comparative accuracy of COLD and S-CCD 2.0 with one varying  
469 parameter and the other two remaining default: i.e.,  $P = 0.99$ ,  $\text{CONSE}=6$ , and  $\lambda=20$ . Both  
470 algorithms exhibit a synchronized response to the change probability threshold (Fig. 5A). The  
471 transition from a loose threshold (0.9) to a strict one (0.9999) results in an equivalent migration  
472 along the error curve for both models. While the COLD algorithm maintains a slightly lower  
473 commission rate at specific intervals, the two curves remain in proximity, suggesting that both  
474 methods are equally capable of being tuned to achieve a desired balance of detection sensitivity.  
475 The peak F1 for both algorithms are also remarkably close, with COLD achieving a maximum  
476 of 0.664 (omission: 33.9%; commission: 33.4%) and S-CCD 2.0 reaching 0.653 (omission:  
477 37.9%; commission: 31.2%). The analysis of the peek window length (Fig. 5B) further  
478 underscores the functional similarity between the two methods. As the confirmation window  
479 expands, both CCDC-like algorithms converge toward a similar “elbow” point. This indicates  
480 that both models utilize temporal consistency in a comparable manner to filter out transient  
481 noise. Fig. 5C examines the influence of the regularization parameter  $\lambda$  on S-CCD 2.0 in  
482 comparison with COLD. Decreasing  $\lambda$  leads to higher commission errors and nonlinear  
483 omission errors in S-CCD 2.0, reflecting the coupled role of  $\lambda$  in controlling both model  
484 regularization and state-space responsiveness. A smaller  $\lambda$  weakens shrinkage and allows the  
485 model to respond more strongly to short-term spectral fluctuations, which can improve  
486 sensitivity to subtle disturbances but also increases the risk of interpreting transient noise as  
487 real change. The nonlinear behavior of omission error suggests that the influence of  $\lambda$  is not  
488 simply proportional to the degree of regularization; rather, it interacts with the Kalman-filter  
489 update process, and residual variance. In contrast, COLD shows a more monotonic trade-off,

490 where reduced regularization is associated with higher commission error and lower omission  
 491 error, indicating greater model flexibility and stronger responsiveness to observations.

492



493

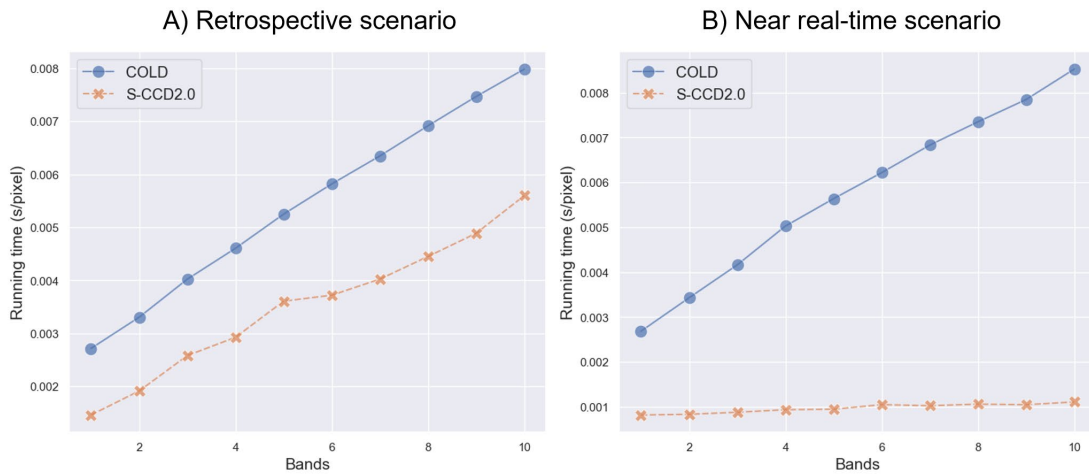
494 **Fig. 5. Accuracy assessment results of COLD and S-CCD 2.0 based on testing dataset ( $n$**   
 495 **= 6,488). A) accuracies under a series of change probability thresholds as 0.9, 0.95, 0.99,**  
 496 **0.999 and 0.9999, under default  $CONSE$  (6) and  $\lambda$  (20). B) accuracies for  $CONSE$**   
 497 **from 4 to 8, under default  $P$  (0.99) and  $\lambda$  (20). C) accuracies for a series of  $\lambda$  as 0, 10,**  
 498 **20, 30 and 40, under default  $P$  (0.99) and  $CONSE$  (6).**

499

500 Fig. 6 compares the computational efficiency of COLD and S-CCD 2.0 under both  
 501 retrospective and NRT scenarios as a function of the number of spectral bands. In the  
 502 retrospective scenario (Fig. 6A), the running time per pixel increases approximately linearly  
 503 with band number for both methods. However, S-CCD 2.0 consistently exhibits lower  
 504 computational cost than COLD across all band configurations, requiring approximately two-  
 505 thirds of the processing time. Moreover, the performance gap widens as the number of bands  
 506 increases, indicating improved scalability of S-CCD 2.0 for multi-band retrospective processing.

507 In the NRT scenario (Fig. 6B), S-CCD 2.0 achieves 3–6 $\times$  faster than COLD. The

508 computational cost of both methods increases with band number; however, the increase for S-  
 509 CCD is much less pronounced than for COLD. Because the baseline processing time of S-CCD  
 510 2.0 is substantially lower, the growth trend with increasing spectral dimensionality is not  
 511 visually prominent at this scale. In contrast, COLD exhibits a clear linear increase in running  
 512 time. These results indicate that S-CCD 2.0 substantially reduces per-update computational  
 513 overhead in NRT monitoring, and that its state-space-based design and jump-update strategy  
 514 effectively mitigate the impact of increasing spectral dimensionality, making it well suited for  
 515 operational NRT applications with high-dimensional spectral inputs.



516  
 517 **Fig. 6. Efficiency comparison between COLD (model updating at each 3% of the**  
 518 **observation number that has not undergone updating with three observations as**  
 519 **minimum) and S-CCD 2.0 based on testing dataset (n = 6488). The length of each time-**  
 520 **series plot was cut into 300 temporal observations. A) Average processing time per pixel**  
 521 **for the retrospective scenario. B) Average processing time per pixel for the NRT scenario.**

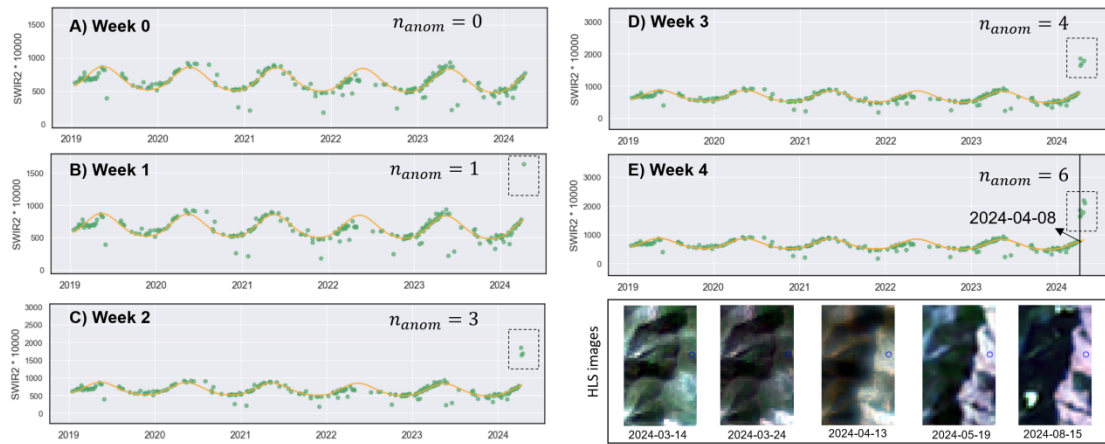
522

## 523 5. Application

---

## 524 5.1 NRT detection for logging

525 Fig. 7 illustrates the NRT monitoring workflow of S-CCD 2.0 using *pyxccd* for a suspected  
526 logging event in Sichuan Province, China, using the SWIR2 time series. At Week 0, the  
527 observations (green dots) are well explained by the fitted seasonal model (orange curve), and  
528 no anomalous points are recorded ( $n_{anom}=0$ ). Beginning at Week 1, an observation at the end  
529 of the series deviates markedly from the expected seasonal trajectory and is flagged as an  
530 anomaly ( $n_{anom}=1$ ). At this time, although no break is detected, S-CCD 2.0 has outputted  
531 anomaly information at the tail, including the number of anomalies, its spectral reflectance, the  
532 current harmonic coefficients (refers to Table A1 for details). As new acquisitions are ingested  
533 (Weeks 2–3), additional high-magnitude deviations accumulate (dashed boxes), increasing the  
534 anomaly count ( $n_{anom}= 3$  to 4), while the harmonic model is only slightly adjusted by Kalman  
535 filter. By Week 4, the sustained and repeated departures from the predicted SWIR2 signal satisfy  
536 the S-CCD 2.0 decision rule, and a structural break is declared (“Break detected”, vertical line;  
537  $n_{anom}= 6$ ). The corresponding image chips (2024-03-14 to 2024-08-15) show progressive  
538 canopy disturbance and exposed ground material at the target location (blue marker), providing  
539 independent visual confirmation that the detected breakpoint (2024-04-08) corresponds to an  
540 active logging disturbance.



541

542 **Fig. 7. An example for S-CCD 2.0 detecting a suspected logging event for an NRT scenario**

543 **at a per-week updating basis in Sichuan, China. While the logging event is fully confirmed**

544 **as a break in Week 4, S-CCD 2.0 starts outputting anomalies since the Week 1.**

545

## 546 5.2 Ecosystem disturbance monitoring

547 Fig. 8 compares S-CCD 2.0 performance when applied to multiple coarse-resolution

548 ecosystem products over the same location, i.e., 500-m NDVI [23], 500-m LAI [24], 0.05-

549 degree SIF [25], and 500-m GPP [26]. For each variable, S-CCD 2.0 fits a model summed from

550 a trimodal (trend + annual + semiannual + four-month) state-space model (orange curve) to the

551 existing observations (green dots), and identifies departures from the expected trajectory as

552 positive/negative anomalies and breaks. Across all products, the dominant annual phenology is

553 captured well despite differing dynamic ranges and noise characteristics, indicating that the

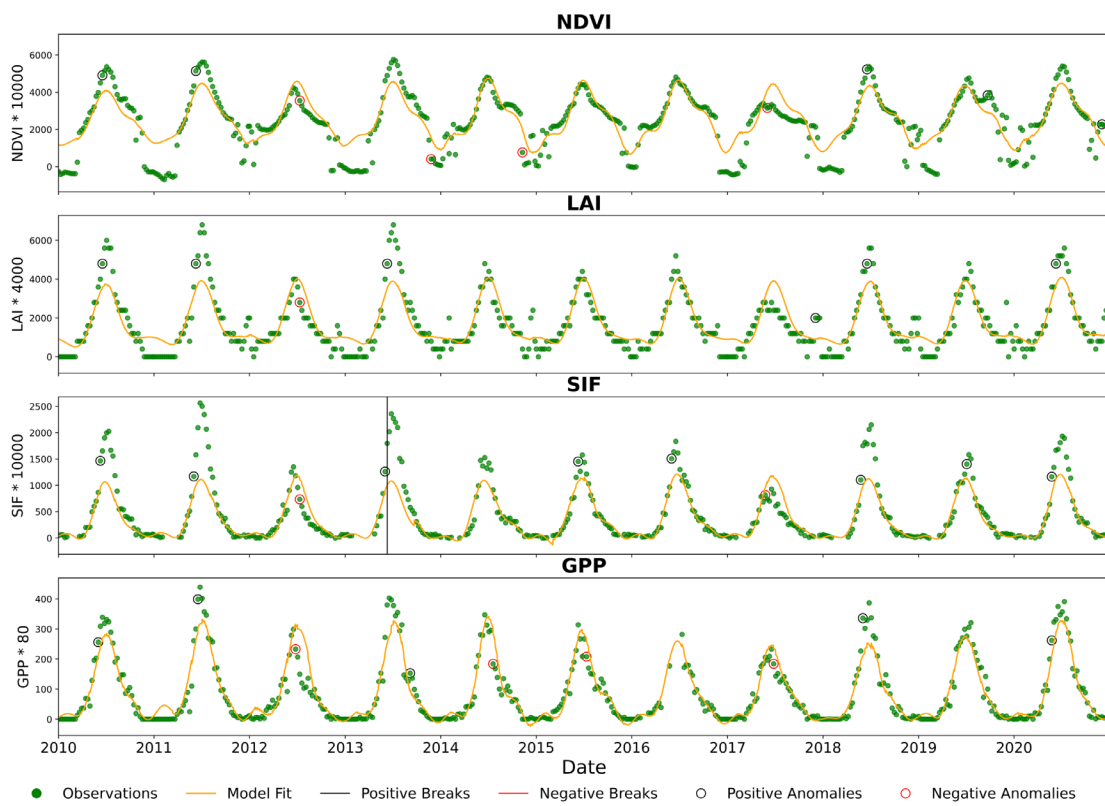
554 state-space framework can accommodate structurally different biophysical signals. Most

555 departures in NDVI, LAI, and GPP occur as isolated anomalies (blue/red open circles) and are

556 not sufficiently persistent to trigger a regime shift, suggesting short-lived perturbations and/or

557 retrieval noise rather than sustained ecosystem change and hence rationale for using “anomaly-

558 break” detection hierarchy. In contrast, the SIF series exhibits a more coherent and sustained  
 559 deviation that leads to a detected structural break (black vertical line), after which subsequent  
 560 observations are evaluated relative to the updated baseline. Overall, this comparison  
 561 demonstrates the transferability of S-CCD 2.0 to diverse coarse-resolution indicators and  
 562 highlights the value of multi-product monitoring, where canopy-structure proxies (NDVI/LAI)  
 563 and functional proxies (SIF/GPP) can show complementary sensitivity to disturbance signals.

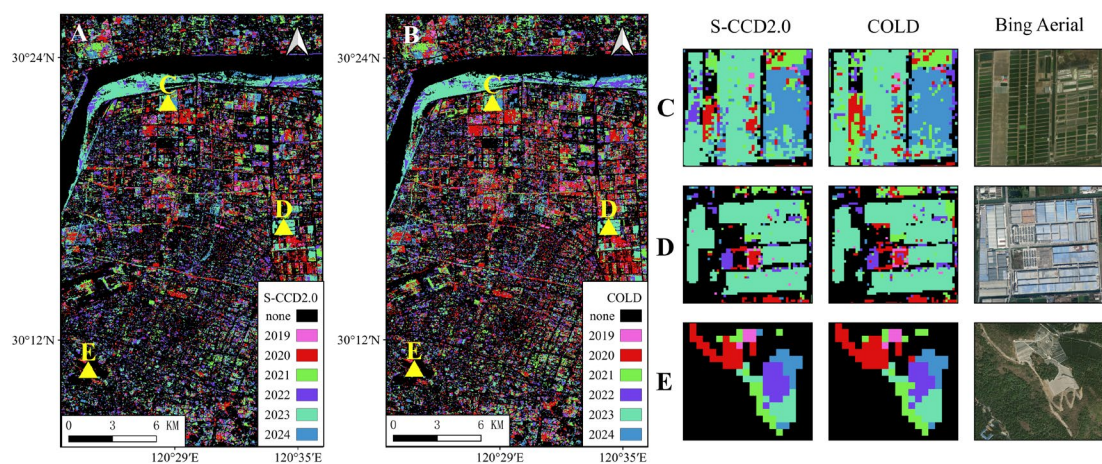


564  
 565 **Fig. 8. Cross-product comparison of S-CCD 2.0 detecting anomalies and breaks for**  
 566 **coarse-resolution ecosystem disturbance monitoring (NDVI, LAI, SIF, and GPP) based**  
 567 **upon a location in Montana, United States.**

568  
 569 **5.3 Large-scale processing**

570 Fig. 9 compares wall-to-wall disturbance mapping results produced by S-CCD 2.0 and

571 COLD using *pyxccd* over a large region (Hangzhou City, China), where each pixel is labeled  
 572 by the recent detected change year (colors for 2019–2024) and unchanged areas are shown in  
 573 black. At the landscape scale, the two methods yield highly consistent spatial patterns and  
 574 similar temporal attribution of disturbance, capturing the same dominant clusters and linear  
 575 features of change across the scene. The three example subsets (C-E) further illustrate this  
 576 agreement at local scales: both S-CCD 2.0 and COLD delineate nearly identical disturbance  
 577 footprints and assign comparable change years, and the detected patterns are visually supported  
 578 by the corresponding Bing Aerial imagery (e.g., land conversion and infrastructure/clearing  
 579 signatures). Differences between the two outputs are limited to scattered, isolated pixels and  
 580 minor boundary variations, which are expected given mixed pixels, temporal sampling  
 581 differences, and retrieval noise. Overall, these results indicate that S-CCD 2.0 achieves  
 582 disturbance mapping performance that is essentially comparable to the established COLD  
 583 approach in large-scale processing, while maintaining close spatial and temporal coherence  
 584 with independent high-resolution reference imagery.



585  
 586 **Fig. 9. Large-Scale Comparison of Disturbance Mapping Between S-CCD 2.0 and COLD**  
 587 **with Aerial Imagery Validation**

---

588

589 **6. Conclusion**

590 This study introduces *pyxccd*, an open-source Python package for scalable, continuous analysis  
591 from satellite-based time series dataset. It integrates high-performance C kernels with a user-  
592 friendly API, supporting COLD and S-CCD 2.0 algorithms. *Pyxccd* improves efficiency,  
593 offering 1.4–1.9× faster processing and practical utility for NRT disturbance detection and  
594 ecosystem monitoring.

595

---

596 **Appendices**

597 **Table A1: the NRT model structure (*nrt\_model*) is retained by S-CCD 2.0 to**  
 598 **analyze the most recent anomalies and enable recursive update of the model**  
 599 **coefficients.**

Element name	Data type	Usage	Description
t_start_since1982	Short	General	The start date of the current segment, formatted as ordinal date – 723742
obs	2-d array	Peek window	The last eight multiband observations.
obs_date_since1982	1-d array	Peek window	The dates for the last eight observations
covariance	2-d array	State-space	Multiband covariance matrix (each 2-d covariance matrix is flatten to 1-d array)
nrt_coefs	2-d array	State-space	Harmonic coefficients converted from states at the last updating date (see Eq. A7-12 in the appendix)
H	1-d array	State-space	Multiband observation noise
rmse_sum	1-d array	RMSE update	Multiband sum of squared errors
num_obs	Short	RMSE update	Current number of clear observations that have been processed
anomaly_conse	Byte	Anomaly analysis	The consecutive anomaly observation number at the tail
cm_angle	Short	Anomaly analysis	The included angle for the anomalies at the tail
norm_cm	Short	Anomaly analysis	The normalized change magnitude for the anomalies at the tail

600

601 **A1. Conversion between harmonic coefficients and states**

602 Converting harmonic coefficients ( $a_0, c_1, a_1, b_1, a_2, b_2$ ) to states ( $\mu_t, v_t, \gamma_{1,t}, \gamma_{1,t}^*, \gamma_{2,t},$

603  $\gamma_{2,t}^*$ ) at time  $t$ :

604 
$$\mu_t = a_0 + c_1 t \quad (A1)$$

605 
$$v_t = c_1 \quad (A2)$$

606 
$$\gamma_{1,t} = a_1 \cos\left(\frac{2\pi}{m} t\right) + b_1 \sin\left(\frac{2\pi}{m} t\right) \quad (A3)$$

---

607  $\gamma_{1,t}^* = -a_1 \sin\left(\frac{2\pi}{m}t\right) + b_1 \cos\left(\frac{2\pi}{m}t\right)$  (A4)

608  $\gamma_{2,t} = a_2 \cos\left(\frac{4\pi}{m}t\right) + b_2 \sin\left(\frac{4\pi}{m}t\right)$  (A5)

609  $\gamma_{2,t}^* = -a_2 \sin\left(\frac{4\pi}{m}t\right) + b_2 \cos\left(\frac{4\pi}{m}t\right)$  (A6)

610

611 Converting states at time  $t$  to harmonic coefficients:

612  $a_0 = \mu_t - c_1 t$  (A7)

613  $c_1 = v_t$  (A8)

614  $a_1 = \gamma_{1,t} \cos\left(\frac{2\pi}{m}t\right) - \gamma_{1,t}^* \sin\left(\frac{2\pi}{m}t\right)$  (A9)

615  $b_1 = \gamma_{1,t} \sin\left(\frac{2\pi}{m}t\right) + \gamma_{1,t}^* \cos\left(\frac{2\pi}{m}t\right)$  (A10)

616  $a_2 = \gamma_{2,t} \cos\left(\frac{4\pi}{m}t\right) - \gamma_{2,t}^* \sin\left(\frac{4\pi}{m}t\right)$  (A11)

617  $b_2 = \gamma_{2,t} \sin\left(\frac{4\pi}{m}t\right) + \gamma_{2,t}^* \cos\left(\frac{4\pi}{m}t\right)$  (A12)

618

## 619 **A2 Key modules of pyxccd**

620 The modules were introduced based upon *pyxccd* v1.0.2, released at Jan. 7, 2026. The  
621 package is distributed through PyPI, requires Python  $\geq 3.9$ , and is licensed under Apache-2.0.

622 (1) Change detection module

623 The *pyxccd.ccd* module is the computational heart of the package, containing functions to  
624 analyze spectral time-series data and detect land-surface changes.

625 *ccd\_detect()*: the primary function for COLD, it analyzes historical land-surface data by  
626 accepting observation dates and spectral inputs. Users can adjust detection parameters,  
627 returning a structured array of temporal segments with metadata, including break dates, model  
628 coefficients, and spectral change magnitudes.

629 *sccd\_detect()*: this function performs the S-CCD 2.0 for retrospective scenarios,

---

630 establishing the initial state-space model and returning a *SccdOutput* structure. It offers optional  
631 outputs, including a data frame of states for each band and an anomaly detection result. Users  
632 can control critical S-CCD parameters, including CONSE, P, conse, p,  $\lambda$ , and interval days for  
633 outputting states.

634 *sccd\_update()*: this function supports NRT monitoring by updating an existing *SccdOutput*  
635 structure using only newly collected data, minimizing memory overhead and computational  
636 cost.

637 *Flexible Variants*: *Pyxccd* includes flexible variants like *cold\_detect\_flex()* and  
638 *sccd\_detect\_flex()*, which allow users to input a wide range of time-series data (e.g., NDVI,  
639 GPP, LAI) and extend the model to support complex ecosystems with multiple growing seasons  
640 through a trimodal harmonic model.

## 641 (2) Land-cover Classification Module

642 The *pyxccd.pyclassifier* module implements the CCDC framework to translate structural  
643 breaks and harmonic coefficients into thematic land-cover maps.

644 Through the *get\_features()* function, the library extracts a high-dimensional feature set  
645 from the *cold\_rec\_cg* or *SccdOutput* structures. These features include the intercept, slope, and  
646 the sine/cosine coefficients of the harmonic cycles for each spectral band. The module is model-  
647 agnostic but includes optimized wrappers for a random-forest classifier, allowing users to train  
648 models on historical data and apply them consistently across a temporal segment until a  
649 structural break is detected.

## 650 (3) Spatial orchestration module

651 The *pyxccd.imagetool* module provides a high-level workflow to scale pixel-based

---

652 algorithms to large-scale geospatial datasets. First, the *prepare\_ard.py* utility handles the pre-  
653 processing and ingestion of time-series images, standardizing multi-temporal image stacks and  
654 quality masks into a format optimized for time-series analysis and partitioning extensive  
655 geographic regions into manageable spatial blocks to enable efficient memory management and  
656 multi-core parallelization. Second, *tile\_processing.py* serves as the primary execution driver.  
657 This script manages the distribution of data to the core *pyxccd.ccd* engines and gathers the  
658 resulting model coefficients and break records. Finally, *export\_change\_map.py* facilitates the  
659 synthesis of these results, mosaicking the processed tiles and translating the raw detection  
660 outputs into standardized geospatial products. This automated pipeline enables researchers to  
661 generate comprehensive raster layers with minimal manual intervention.

#### 662 (4) Utilities and data integration module

663 The *pyxccd.common* and *pyxccd.utils* modules provide standardized Python data structures,  
664 including *anomaly\_dt* and *cold\_rec\_cg*, for consistent data handling across algorithms. These  
665 utilities support conversion, validation, and export of algorithm outputs for external analysis  
666 tools and mapping workflows.

667

### 668 **CRedit authorship contribution statement**

669 S. Y.: Writing – original draft, Validation, Software, Methodology, Formal analysis, Supervision,  
670 Funding acquisition, Conceptualization. Y. H.: Writing – review & editing, Validation, Software.  
671 T. C.: Visualization, Validation.

672

### 673 **Data availability statement**

---

674 The *pyxccd* source code is publicly available through PyPI and GitHub [27]. The package  
675 version described in this manuscript is V1.0.2. The data that support the findings of this study  
676 are available from the corresponding author, S.Y., upon request.

677

## 678 **Conflict of Interest statement**

679 The authors declare that they have no known competing financial interests or personal  
680 relationships that could have appeared to influence the work reported in this paper.

681

## 682 **Funding information**

683 The authors are grateful for the financial support provided by Major Science and Technology  
684 Collaboration Program of Zhejiang Province (2025SNJF012) and National Natural Science  
685 Foundation of China (42401393).

686

687

## 688 **Reference**

- 689 [1] Z. Zhu, “Change detection using landsat time series: A review of frequencies,  
690 preprocessing, algorithms, and applications,” *ISPRS J. Photogramm. Remote Sens.*, vol.  
691 130, pp. 370–384, 2017.
- 692 [2] S. Ye *et al.*, “Detecting subtle change from dense Landsat time series: Case studies of  
693 mountain pine beetle and spruce beetle disturbance,” *Remote Sensing of Environment*,  
694 vol. 263. 2021. doi: 10.1016/j.rse.2021.112560.
- 695 [3] J. E. Vogelmann, A. L. Gallant, H. Shi, and Z. Zhu, “Perspectives on monitoring gradual  
696 change across the continuity of Landsat sensors using time-series data,” *Remote Sens.*

- 
- 697        *Environ.*, vol. 185, pp. 258–270, 2016.
- 698 [4] Z. Zhu, S. Qiu, and S. Ye, “Remote sensing of land change: A multifaceted perspective,”
- 699        *Remote Sens. Environ.*, vol. 282, p. 113266, 2022.
- 700 [5] C. E. Woodcock, T. R. Loveland, M. Herold, and M. E. Bauer, “Transitioning from
- 701        change detection to monitoring with remote sensing: A paradigm shift,” *Remote Sens.*
- 702        *Environ.*, vol. 238, p. 111558, 2020.
- 703 [6] H. West, N. Quinn, and M. Horswell, “Remote sensing for drought monitoring & impact
- 704        assessment: Progress, past challenges and future opportunities,” *Remote Sens. Environ.*,
- 705        vol. 232, p. 111291, 2019.
- 706 [7] C. F. Brown *et al.*, “Dynamic World, Near real-time global 10 m land use land cover
- 707        mapping,” *Sci. Data*, vol. 9, no. 1, pp. 1–17, 2022.
- 708 [8] S. Ye, Z. Zhu, and J. W. Suh, “Leveraging past information and machine learning to
- 709        accelerate land disturbance monitoring,” *Remote Sens. Environ.*, vol. 305, p. 114071,
- 710        2024.
- 711 [9] G. Welch and G. Bishop, “An introduction to the Kalman filter,” 1995.
- 712 [10] R. S. Tsay, *Analysis of financial time series*. John wiley & sons, 2005.
- 713 [11] Z. Zhu and C. E. Woodcock, “Continuous change detection and classification of land
- 714        cover using all available Landsat data,” *Remote Sens. Environ.*, vol. 144, pp. 152–171,
- 715        2014.
- 716 [12] M. A. Friedl *et al.*, “Medium spatial resolution mapping of global land cover and land
- 717        cover change across multiple decades from landsat,” *Front. Remote Sens.*, vol. 3, p.
- 718        894571, 2022.

- 
- 719 [13] X. Zhang, L. Liu, X. Chen, Y. Gao, S. Xie, and J. Mi, “GLC\_FCS30: Global land-cover  
720 product with fine classification system at 30 m using time-series Landsat imagery,”  
721 *Earth Syst. Sci. Data Discuss.*, vol. 2020, pp. 1–31, 2020.
- 722 [14] J. F. Brown *et al.*, “Lessons learned implementing an operational continuous United  
723 States national land change monitoring capability: The Land Change Monitoring,  
724 Assessment, and Projection (LCMAP) approach,” *Remote Sensing of Environment*. p.  
725 111356, 2019. doi: 10.1016/j.rse.2019.111356.
- 726 [15] G. Z. Xian *et al.*, “Implementation of the CCDC algorithm to produce the LCMAP  
727 Collection 1.0 annual land surface change product,” *Earth Syst. Sci. Data*, vol. 14, no. 1,  
728 pp. 143–162, 2022.
- 729 [16] S. Ye, Z. Zhu, and G. Cao, “Object-based continuous monitoring of land disturbances  
730 from dense Landsat time series,” *Remote Sens. Environ.*, vol. 287, p. 113462, 2023.
- 731 [17] P. Arévalo, E. L. Bullock, C. E. Woodcock, and P. Olofsson, “A suite of tools for  
732 continuous land change monitoring in google earth engine,” *Front. Clim.*, vol. 2, p.  
733 576740, 2020.
- 734 [18] Z. Zhu *et al.*, “Continuous monitoring of land disturbance based on Landsat time series,”  
735 *Remote Sens. Environ.*, vol. 238, p. 111116, 2020.
- 736 [19] S. Ye, J. Rogan, Z. Zhu, and J. R. Eastman, “A near-real-time approach for monitoring  
737 forest disturbance using Landsat time series: stochastic continuous change detection,”  
738 *Remote Sensing of Environment*, vol. 252. 2021. doi: 10.1016/j.rse.2020.112167.
- 739 [20] Z. Zhu and C. E. Woodcock, “Object-based cloud and cloud shadow detection in  
740 Landsat imagery,” *Remote Sens. Environ.*, vol. 118, pp. 83–94, 2012.

- 
- 741 [21] M. Claverie, E. F. Vermote, B. Franch, and J. G. Masek, “Evaluation of the Landsat-5  
742 TM and Landsat-7 ETM+ surface reflectance products,” *Remote Sens. Environ.*, vol.  
743 169, pp. 390–403, 2015.
- 744 [22] W. B. Cohen *et al.*, “Forest disturbance across the conterminous United States from  
745 1985–2012: The emerging dominance of forest decline,” *For. Ecol. Manage.*, vol. 360,  
746 pp. 242–252, 2016.
- 747 [23] C. Schaaf and Z. Wang, “MODIS/Terra+ aqua BRDF/Albedo nadir BRDF adjusted ref  
748 daily L3 global-500m V061,” *NASA EOSDIS L. Process. Distrib. Act. Arch. Cent. data*  
749 *set*, p. MCD43A4-061, 2021.
- 750 [24] R. Myneni, Y. Knyazikhin, and T. Park, “MODIS/Terra Leaf Area Index/FPAR 8-Day  
751 L4 Global 500m SIN Grid V061,” *NASA EOSDIS L. Process. Distrib. Act. Arch. Cent.*  
752 *data set*, p. MOD15A2H-061, 2021.
- 753 [25] X. Li and J. Xiao, “A global, 0.05-degree product of solar-induced chlorophyll  
754 fluorescence derived from OCO-2, MODIS, and reanalysis data,” *Remote Sens.*, vol. 11,  
755 no. 5, p. 517, 2019.
- 756 [26] D. A. Sims *et al.*, “A new model of gross primary productivity for North American  
757 ecosystems based solely on the enhanced vegetation index and land surface temperature  
758 from MODIS,” *Remote Sens. Environ.*, vol. 112, no. 4, pp. 1633–1646, 2008.
- 759 [27] Remote-Sensing-of-Land-Resource-Lab, 2026. pyxccd v1.0.2 [software]. GitHub/PyPI.  
760 <https://github.com/Remote-Sensing-of-Land-Resource-Lab/pyxccd> (accessed 19 May  
761 2026).
- 762